Available online at www.sciencedirect.com

jmr&t Journal of Materials Research and Technology

www.jmrt.com.br

Original Article

Plate-like growth in a eutectic Bi–Ni alloy: effects of morphological microstructure evolution and Bi_3Ni intermetallic phase on tensile properties

Clarissa Cruz, Thiago Lima, Rafael Kakitani, André Barros, Amauri Garcia, Noé Cheung *

Department of Manufacturing and Materials Engineering, University of Campinas – UNICAMP, 13083-860 Campinas, SP, Brazil

ARTICLE INFO

Article history:
Received 23 November 2019
Accepted 3 March 2020
Available online 10 April 2020

Keywords:
Thermal interface materials
Bi–Ni eutectic
Solidification
Microstructure
Tensile properties

ABSTRACT

The development of efficient thermal interface materials (TIMs) has become an emerging demand mainly driven by the continual rise in power dissipation of high-performance microprocessors. In this context, Bi-based alloys are among the promising types of TIMs for electronic packaging applications. However, the influence of the microstructural arrangement on mechanical strength of Bi–Ni alloys remains barely understood. To overcome this issue, this study aims to develop quantitative microstructure features-tensile properties correlations for a Bi–0.28 wt.%Ni alloy solidified in a wide range of cooling rates ($\dot{T}$). In addition to the phase diagram calculated by the Thermo-Calc software (SSOL6 database) and differential scanning calorimetry analysis, the characterization of the Bi_3Ni intermetallic compound is carried out using X-ray diffraction and SEM microscopy with energy dispersive X-ray spectroscopy. Wavy instabilities in the plate-like morphology of the Bi matrix are shown to occur for $\dot{T} \leq 0.13\,^{\circ}C/s$. Besides that, more significant variations in yield and ultimate tensile strengths, σ_y and σ_u, respectively, are associated with a certain range of microstructural spacings between Bi plates (λ) from 47.6 to 135.2 μm. Hence, Hall–Petch type relations are proposed to describe the variation of both σ_y and σ_u as a function of λ.

1. Introduction

Continuous innovation in the electronics industry, increasing functionality of personal electronic devices, and significant miniaturization of integrated circuits are some factors that have driven studies on thermal management technologies to ensure reliable operation and to enhance the lifetime of electronic components, such as highly integrated central processing units (CPUs), light-emitting diodes (LEDs) products, and energy harvesting systems [1,2]. To avoid electronic devices working under overheating conditions, thermal interface materials (TIMs) have been commonly used between a heat-generating device (microprocessor and semiconductor chips for instance) and a heat dissipating device (e.g. heat sink)

* *Corresponding author.*
E-mail: cheung@fem.unicamp.br (N. Cheung).

https://doi.org/10.1016/j.jmrt.2020.03.013

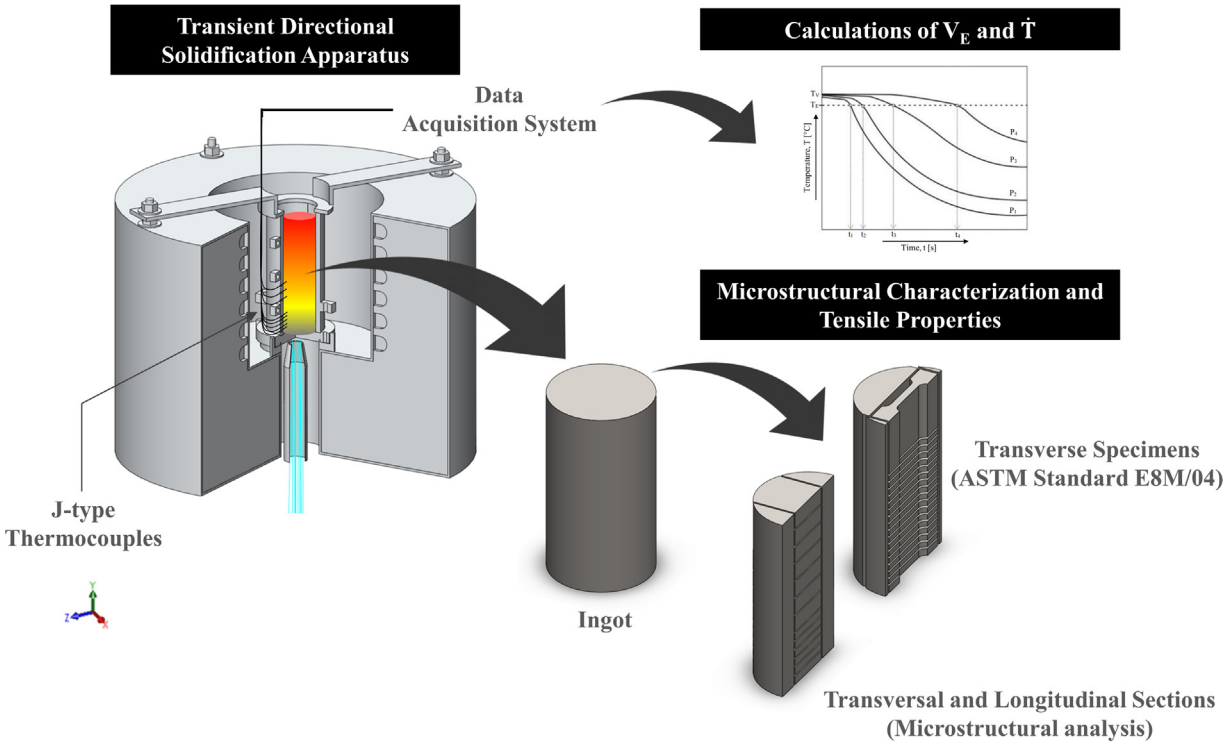

Fig. 1 – Schematic representation of the experimental methods used in the present study.

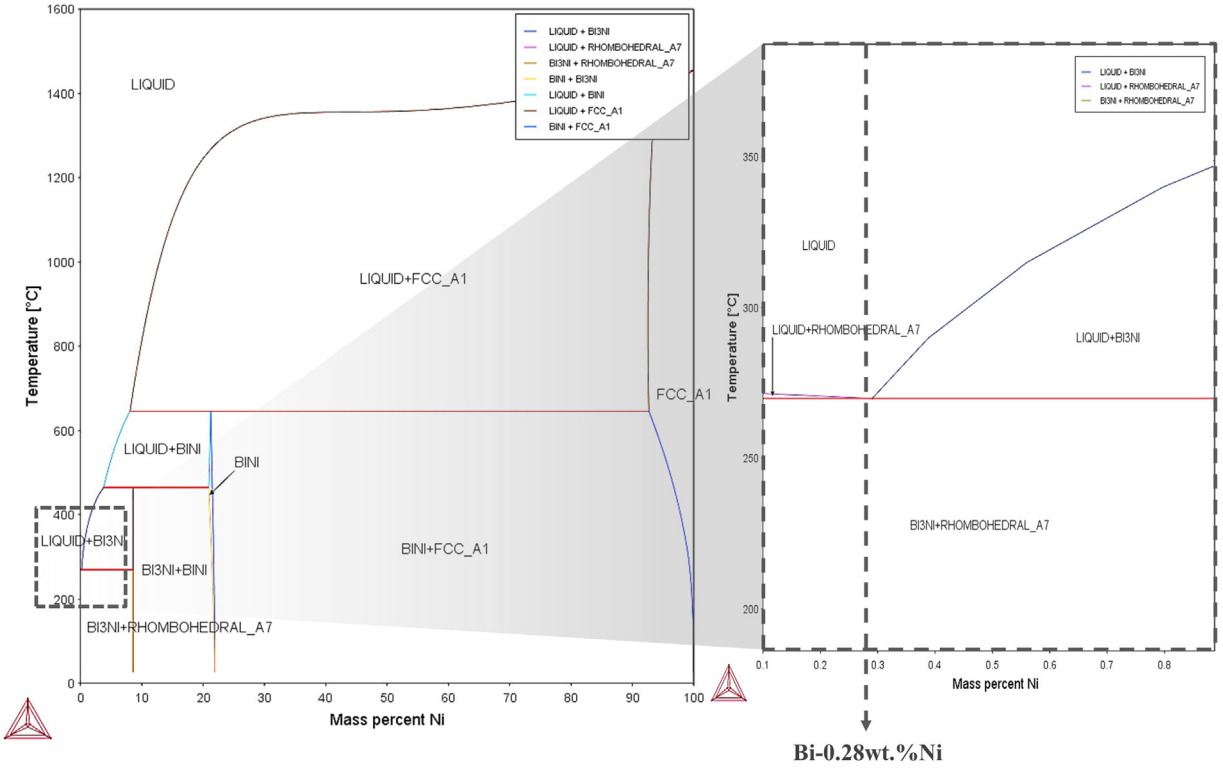

Fig. 2 – (a) Bi–Ni binary phase diagram calculated by the Thermo-Calc software (SSOL6 database). (b) Partial Bi–Ni phase diagram emphasizing the eutectic alloy.

to fill in air gaps, which act as a barrier to heat transfer, improving the thermal coupling [3,4]. However, with the rise in power density due to shrinking feature sizes in electronics, effective heat removal may become a critical issue for the progress in communication, energy harvesting, information, and lighting technologies [4]. Hence, developing new TIMs with enhanced performance has been crucial to meet the thermal management requirements of next-generation electronics.

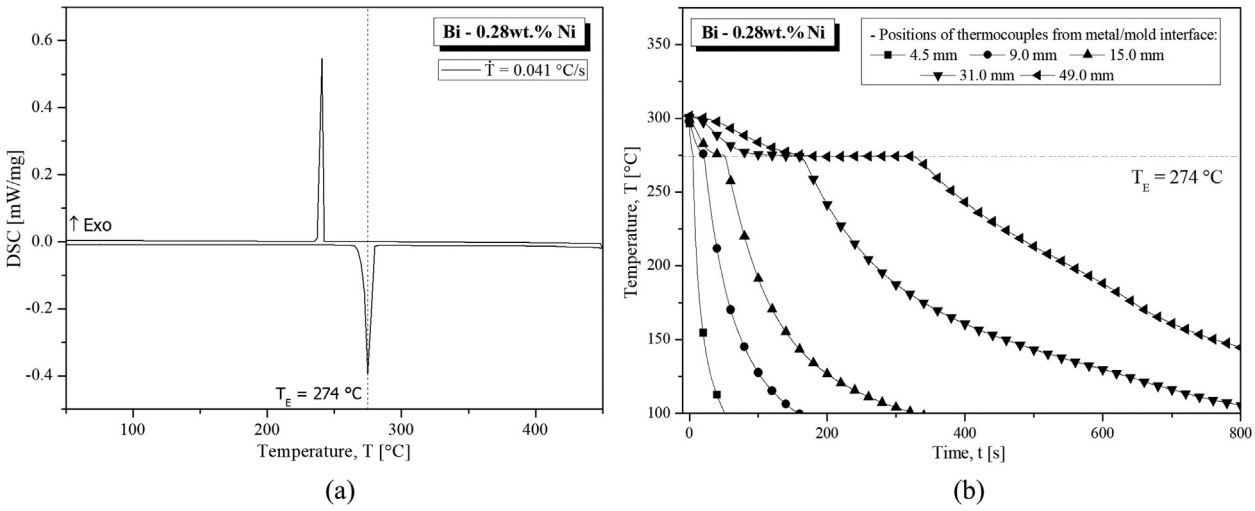

Fig. 3 – (a) DSC profile of the eutectic Bi–Ni alloy and (b) cooling curves recorded along the length of the ingot during directional solidification.

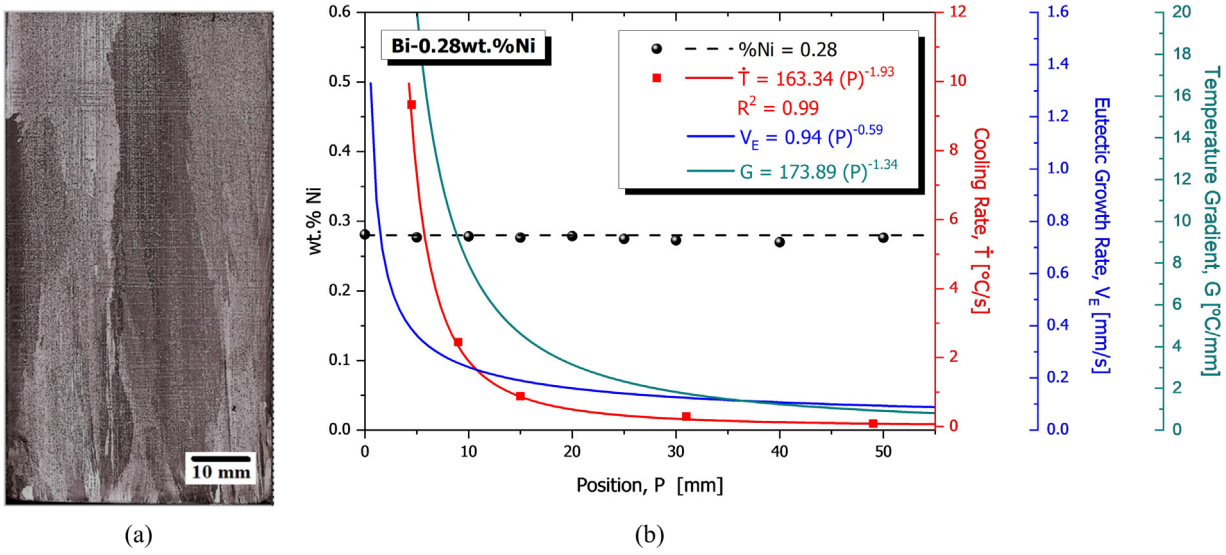

Fig. 4 – (a) Macrostructure and (b) Ni concentration, $\dot{T}$, and V_E profiles as a function of position (P) from the cooled bottom to the top of the Bi–0.28 wt.%Ni alloy ingot.

TIMs may be classified as thermal grease, metallic TIMs, conductive elastomer TIMs, phase-change materials, and emerging TIMs such as composites, polymer solder hybrid, or smart TIMs [5]. Among the several types of TIMs available, both commercially as well as in the research and development phase, low-melting temperature alloys (LMAs), typically composed of In, Ga, Sn, and Bi, have drawn attention because besides offering low thermal resistances at small contact pressure and at a thin bond line, they have also high thermal conductivity as compared to traditional polymeric TIMs [5–8]. Gao and Liu [7], for example, reported thermal interface resistance as low as 2.6 $mm^2\,kW^{-1}$ with a pressure of 0.05 MPa for a Ga-based TIM, which is an order lower than that of the best commercialized thermal greases. On the other hand, despite LMAs offer low thermal interfacial resistance, interfacial reactions with substrates may lead to a gradual decrease in performance and eventual failure. Analyzing two types of LMAs sandwiched on both sides with Cu after different stages of aging, Yang et al. [9] concluded that: (i) while the thermal resistance of a 17Sn51In32Bi alloy remained almost constant, the thermal resistance of a 17Sn26In57Bi alloy increased by about 51% after 800-h aging and (ii) the degradation of the thermal performance of the investigated LMAs TIMS was attributed to the interfacial reaction between Cu and the molten LMAs. Given this strategic importance of LMAs, a comprehensive characterization of such alloys is, therefore, not only of scientific but also of technological interest aiming to improve their performance as TIMs.

A thermal interface resistance as low as 0.253 $mm^2\,kW^{-1}$ has been reported for a TIM consisting of an array of Hg

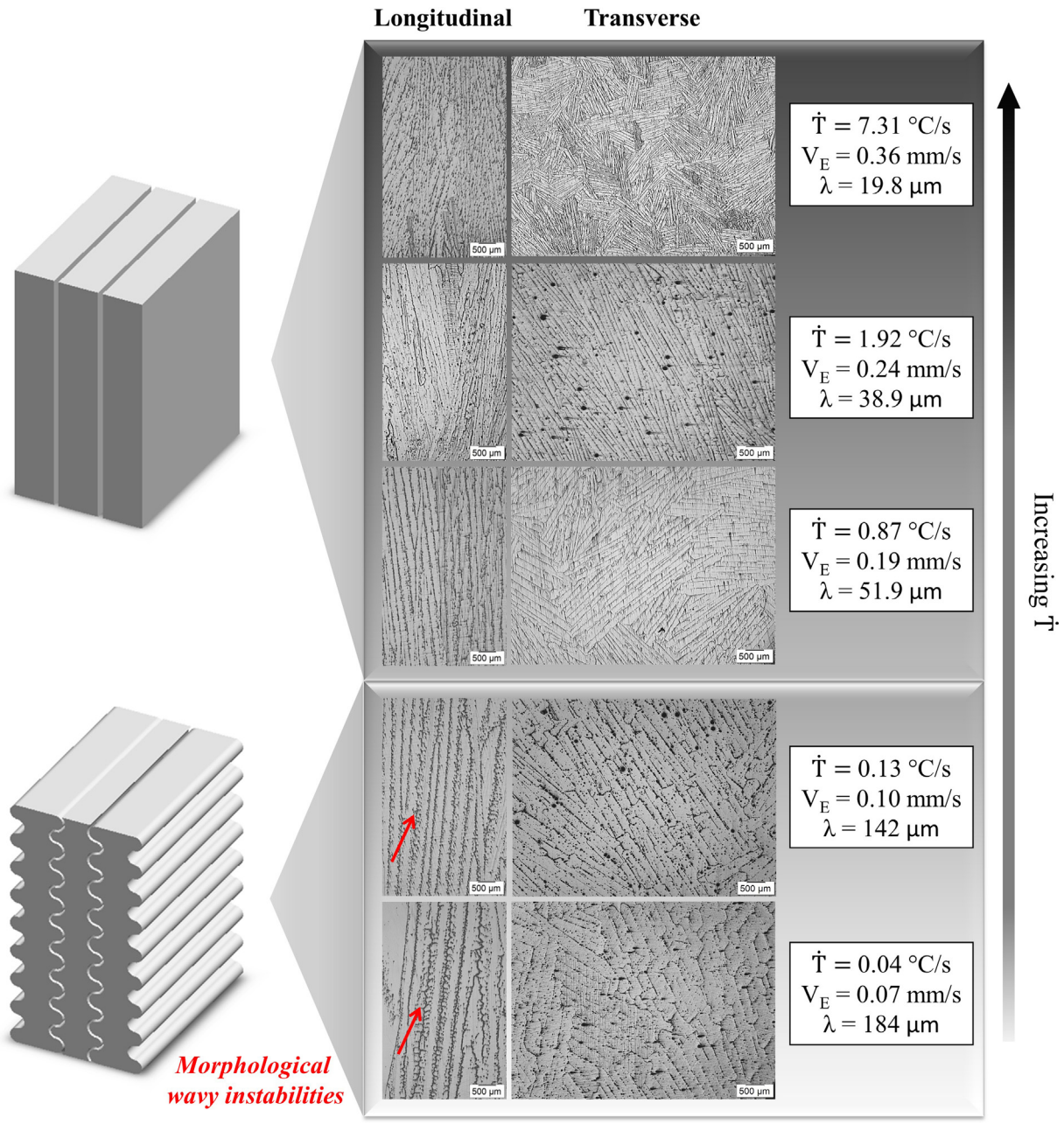

Fig. 5 – Representative longitudinal (left-side) and transverse (right-side) microstructures along the length of the eutectic Bi–Ni alloy ingot.

microdroplets deposited on a silicon die [10]; however, like Cd and Pb, Hg is a hazardous substance and should be avoided due to its toxicity and environmental effects [11]. Compared with these elements, Bi is both environmental and health friendly. In fact, owing to its unique chemical properties, Bi has also been suggested for various applications as a thermoelectric material [12], optical and electro-optical devices [13], hall sensors [14], hydrophobic surfaces [15], as well as lubricant materials [16]. As stated by Septimio et al. [17], a critical issue in developing new Bi-based alloys is the enhancement of a specific property without promoting deleterious effects in another one. Despite some reports in the literature have evaluated the processing/microstructure/property correlations in Bi–Ag [18,19], Bi–Zn [20], Bi–Sb [21], and Bi–In–Sn [22], the literature is still scarce on publications detailing such correlations in new Bi-based alloys suitable for applications as TIMs, focusing on the effects of the interaction of the Bi-rich phase and intermetallic particles on the resulting properties.

Assessing both interfacial morphology and tensile properties of joints between Bi–Ag alloys and two metallic substrates, Cu and Ni, Song et al. [23] have reported that the formation and the morphology of the Bi_3Ni intermetallics have a strong influence on the tensile strength and fracture morphology of the Bi-Ag/Ni joints. Overall, despite intermetallic compounds (IMCs) in joints are considered to be beneficial for the purpose of wetting and bonding, massive growth of brittle IMCs may

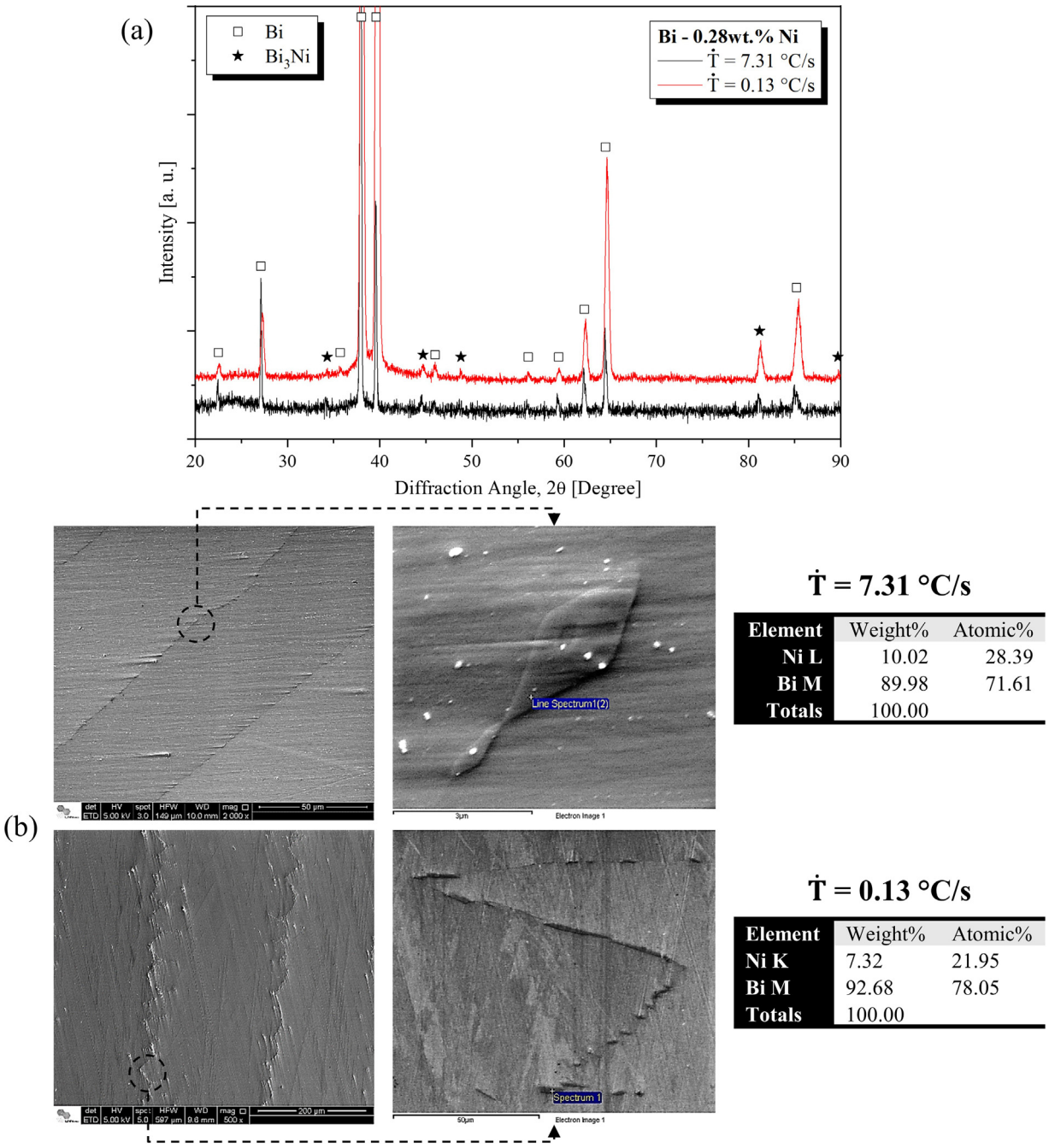

Fig. 6 – (a) XRD patterns and (b) SEM-EDS point microanalysis at different positions in the Bi–0.28 wt.%Ni ingot referring to samples with ($\dot{T}$ = 0.13 °C/s) and without ($\dot{T}$ = 7.31 °C/s) wavy instabilities in the Bi matrix.

cause early bond failure [24]. By examining the Bi-Ni phase diagram, it can be seen that Bi and Ni do not form solid solutions; however, two IMCs, Bi_3Ni and BiNi may be formed. According to Sheikhi and Cho [25], Bi_3Ni is softer and more brittle than BiNi. Dybkov and Duchenko [26] reported a rapid reaction at the Ni-Bi interface at 150, 200 and 250 °C, which resulted in the formation of Bi_3Ni; however, no BiNi IMCs was observed. While Lee et al. [27] demonstrated by the cracks formed along the edges of the indentation mark that the Bi_3Ni phase is quite brittle, such compound has also been known to be a superconductor [28,29]. Considering such interesting physical characteristics, a better understanding on the effects of morphology, size, volume fraction, and distribution of BiNi and Bi_3Ni IMCs throughout the Bi matrix on the properties of Bi–Ni alloys may open new perspectives to the development of new TIMs based on such alloys.

Due to the low yield strength of low melting point metals and their related alloys, they can be easily deformed and, consequently, there is a risk of flowing out during the attachment process, which might result in short circuits during operation of electronic devices [4]. Furthermore, because of their susceptibility to severe distortion during both handling and

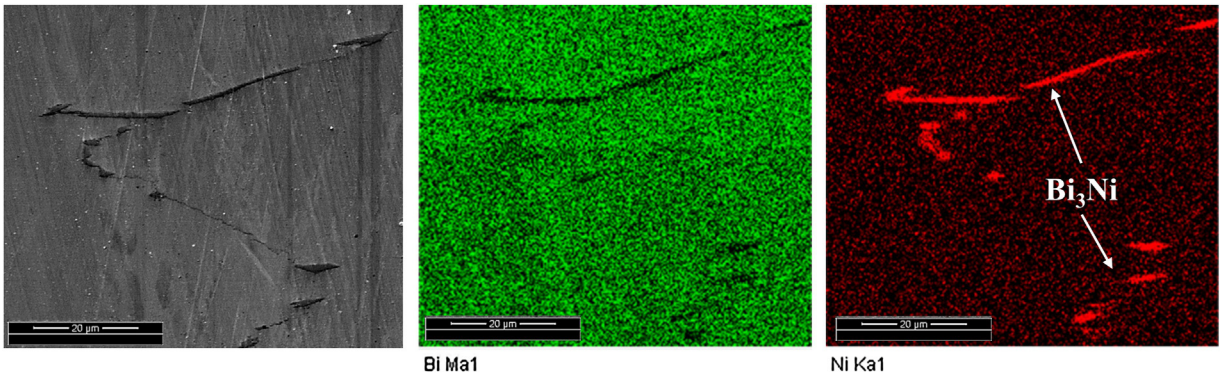

Fig. 7 – Elemental SEM–EDS mapping showing Bi_3Ni particles at the contours of Bi plates.

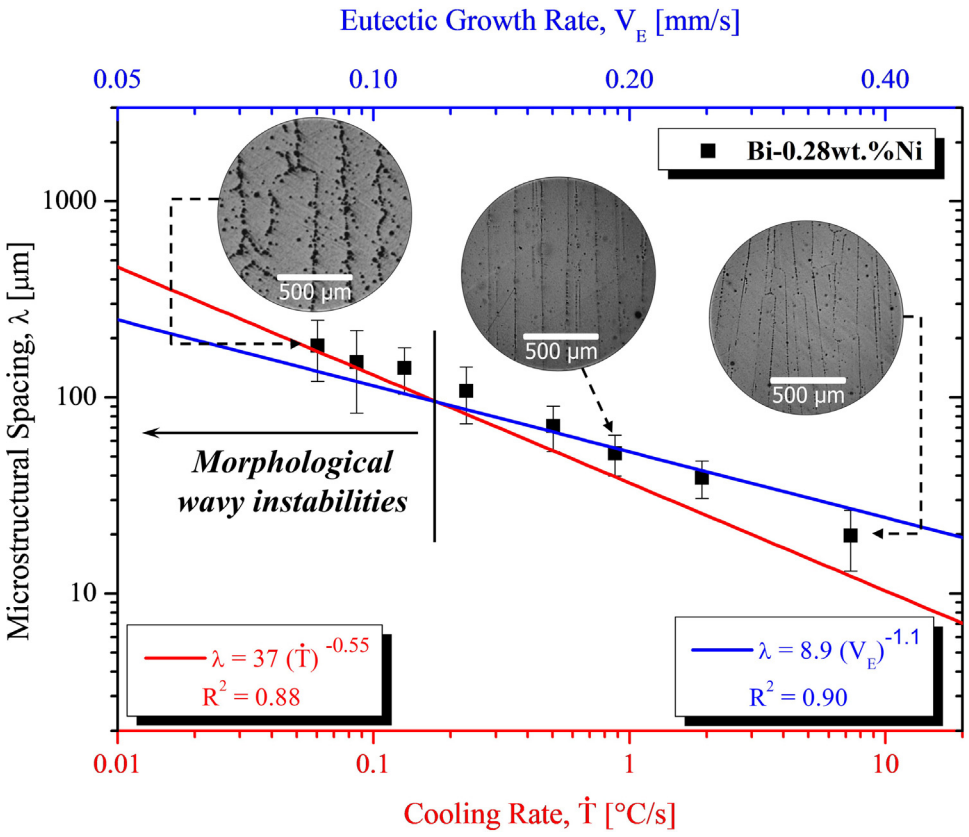

Fig. 8 – Microstructural spacing between the Bi plates as a function of both V_E and $\dot{T}$.

use, just the attachment of a heat sink is typically enough to completely collapse the joints [30]. Considering the challenge to overcome this significant drawback, as well as the great potential of Bi-Ni alloys for application as TIMs, the goal of the present contribution is to investigate the microstructure evolution of a eutectic Bi–0.28 wt.%Ni alloy in a wide range of solidification cooling rates, establishing correlations between microstructural parameters and both yield and ultimate tensile strengths.

2. Experimental procedure

The studied eutectic Bi–0.28 wt.%Ni alloy was prepared from commercially pure Bi (containing 0.0007 wt.%Pb, 0.001 wt.%Cd, 0.001 wt.%Sn, 0.0027 wt.%Ag, and <0.0001 wt.%Fe) and Ni (containing 0.002 wt.%Pb, 0.002 wt.%S, 0.017 wt.%Co, and 0.0040 wt.%Fe). The experimental solidification setup used to obtain the samples was designed in such a way that heat was extracted only through the water-cooled bottom leading to vertically upward growth, as described in previous papers [31,32]. A schematic illustration in Fig. 1 provides a general sequence of the experimental steps with some detailing information included.

When the thermocouple closest to the chilled base measured a temperature of about 301 °C – approximately 10% above of the eutectic temperature (274 °C) – the electrical windings were disconnected, and the water flow was immediately initiated, thus permitting the onset of the directional

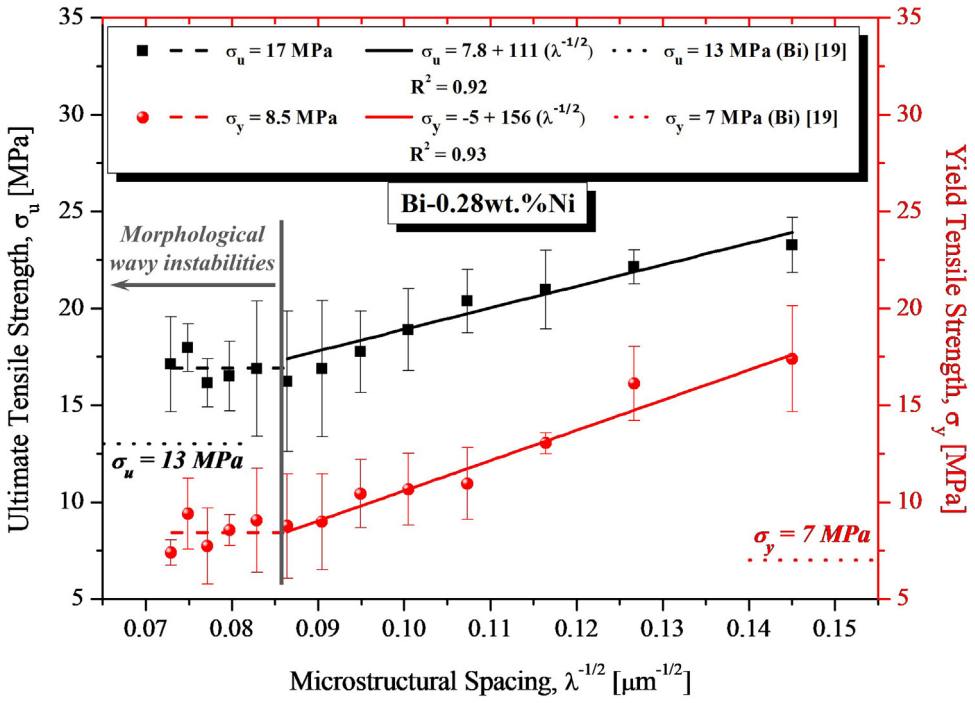

Fig. 9 – Yield and ultimate tensile strengths as a function of the microstructural spacing.

solidification. Well-known experimental techniques [33–36] were applied to calculate both cooling rate ($\dot{T}$) and eutectic growth rate (V_E) using the temperature-time data recorded by a set of five fine type J thermocouples positioned along the length of the directionally solidified ingot.

The resulting cylindrical ingot was sectioned along its vertical axis, grounded and etched with a solution of aqua regia reagent (3HCl:1HNO_3) to reveal the macrostructure. Metallographic samples were extracted from different longitudinal and transverse sections along the length of the directionally solidified ingot to assess the microstructure evolution from the cooled bottom to the top. No etching was necessary for microstructural characterization of these samples. The examination of the microstructure was carried out using optical microscopy (Olympus GX41), scanning electronic microscopy – SEM (Inspect F50) coupled with energy dispersive spectrometer – EDS (Oxford-X-MAX), and X-ray diffraction – XRD (Panalytical X'Pert PRO MRD XL). The line intercept method [37,38] was used for measuring the microstructural spacing (λ) between Bi plates on transverse sections of as-solidified microstructures. Moreover, thermal analysis was performed using a differential scanning calorimeter (DSC) Netzsch, model 200 F3 Maia. The Ni concentration of each sample was determined by using a Rigaku Rix 3100 X-ray Fluorescence Spectrometer. Finally, the specimens were subjected to tensile tests using a MTS 810-FlexTest 40 machine, according to specifications of the ASTM Standard E 8M/04 at a strain rate of $10^{-3}\,s^{-1}$.

3. Results and discussion

According to the Bi–Ni phase diagram calculated by the Thermo-Calc software and shown in Fig. 2, Bi and Ni do not form solid solutions; however, Bi_3Ni and BiNi IMCs may be formed. It is also noted three invariant reactions: LIQUID + FCC_A1(Ni) ↔ BINI at 614 °C (peritectic), LIQUID + BINI ↔ BI3NI at 470 °C (peritectic), and LIQUID ↔ BI3NI + RHOMBOHEDRAL_A7(Bi) at 274 °C (eutectic). Overall of the mixing ratios for Bi and Ni, the Bi–Ni eutectic composition (investigated in this work) has the lowest possible melting temperature, as expected. Moreover, the DSC experimental curve for the Bi–0.28 wt.%Ni alloy at a cooling rate of 0.041 °C/s (Fig. 3(a)) confirms that 274 °C is the temperature at which the eutectic transformation occurred. Phase change can also be noticed through slope changes of the cooling curves at 274 °C, as can be seen in Fig. 3(b), for the Bi–0.28 wt.%Ni alloy.

The typical resulting macrostructure of the directionally solidified ingot is depicted in Fig. 4(a). It can be seen that a columnar macrostructure prevailed along the entire length of the investigated eutectic Bi–Ni alloy ingot presenting the columnar grains aligned to the heat flow direction, without trace of columnar-to-equiaxed transition. By analyzing the experimental solidification thermal parameters shown in Fig. 4(b), it can be noted that both $\dot{T}$, V_E and thermal gradient ($G = \dot{T}/V_E$) profiles vary significantly along the length of the ingot. Higher growth rate and cooling rate values are associated with positions near to the cooled interface; however, with the advance of the solidification front, decreasing profiles of both thermal parameters are observed, as expected. Furthermore, no evidences of macrosegregation is observed for the Bi–0.28 wt.%Ni alloy along the casting (Fig. 4(b)), i.e., the solute concentration remains essentially the same and close to that of the alloy nominal composition for all analyzed samples.

Representative longitudinal and transverse micrographs are shown in Fig. 5 to elucidate both the Bi matrix morphological evolution and the scale of the microstructure

along the ingot length. It can be seen arrays of parallel plates, i.e., a particular Bi matrix plate-like morphology as the characteristic pattern along the entire length of the Bi–0.28 wt.%Ni alloy ingot. Despite such morphology seems to be unexpected in terms of as-solidified microstructures of metallic alloys, the occurrence of plate-like structures has been already reported in some other solidification studies involving Sn–Sb alloys [39] as well as Zn-based alloys in both Bridgman type [40–43] and unsteady-state solidification experiments [44–46]. The main difference observed herein is associated with the morphology of the Bi plates for $\dot{T} \leq 0.13\,^{\circ}C/s$. In addition to coarsening of the microstructure, it can be noted the onset of morphological wavy instabilities in the ingot regions where a regime of lower cooling rates is operative, as indicated by arrows in Fig. 5. Such behavior suggests a partial morphological transition in which the cooling rate is believed to be the critical factor. Similar observation was reported by Santos et al. [44] for Zn–Sn alloys. The authors observed that the combination of lower cooling rates with the increase in the alloy solute content tends to favor even more the development of lateral instabilities of the Zn-rich plates, which progresses toward a morphological transition from a vertical plate-like cell to a sequence of cylindrical-type horizontal cells. It is important to highlight that morphological formation during solidification of alloys is strongly dependent on the anisotropy of the solid–liquid interface energy, on the thermal parameters and on the crystalline structure of the involved elements [47–49].

As can be seen in Fig. 6(a), XRD diffraction patterns at two different positions along the length of the directionally solidified ingot, representing a high and a low level of $\dot{T}$, reveal the occurrence of both Bi and Bi_3Ni. Although the solidification conditions were far from equilibrium, neither BiNi IMC nor Ni has been detected. Due to the texture resulted from directional solidification, no clear analysis of tendencies regarding the intensities of peaks for the different positions from the casting cooled surface can be taken. Moreover, Fig. 6(b) presents SEM micrographs EDS point microanalysis, for the samples solidified at $\dot{T} = 0.13\,^{\circ}C/s$ and $\dot{T} = 7.31\,^{\circ}C/s$, i.e., specimens with and without wavy instabilities in Bi plates, respectively. In both cases, it has been revealed the presence of Bi_3Ni IMC between the Bi plates. A typical SEM-EDS elemental mapping in Fig. 7 presents the distribution of Bi and Ni around the contours of Bi plates, showing Bi_3Ni particles.

In Fig. 8, the microstructural spacing between Bi plates (λ) is plotted as a function of both V_E and $\dot{T}$. Each average λ value has been determined along with its standard variation. In addition, the coefficients of determination (R^2) are inserted to represent how close the experimental scatter is to the fitted regression line. It is observed that despite the formation of morphological wavy instabilities in Bi plates at $\dot{T} \leq 0.13\,^{\circ}C/s$, the power-type experimental laws represented by $\lambda = 8.9(V_E)^{-1.1}$ and $\lambda = 37(\dot{T})^{-0.55}$ can represent the λ evolution for the eutectic Bi–Ni alloy. Similar exponents have also been observed in experimental studies concerning the growth of regular cells and dendrites for metallic binary alloys [50–52]. As mentioned before, as the $\dot{T}$ values are high nearby the cooled bottom of the ingot and decrease toward the top, the λ values increase accordingly.

The tensile properties dependence on the evolution of the scale of the microstructure along the length of the ingot is shown in Fig. 9. It can be seen the effect of both microstructural spacing (λ) and morphological wavy instabilities on yield (σ_y) and ultimate (σ_u) tensile strengths. While these tensile properties remain practically constants in the region of morphological wavy instabilities (coarser microstructure, $\lambda \geq 142\,\mu m$), the aforementioned mechanical properties are affected by the length scale of the microstructure in a range of λ values varying from $47.6\,\mu m$ ($0.145\,\mu m^{-1/2}$) to $135.2\,\mu m$ ($0.086\,\mu m^{-1/2}$). Thus, Hall–Petch-types correlations are proposed relating the more significant variations in σ_y and σ_u with $\lambda^{-1/2}$ in the range: $0.086\,\mu m^{-1/2} < \lambda^{-1/2} < 0.145\,\mu m^{-1/2}$. The Hall–Petch law was originally established to relate σ_y to the grain size of polycrystalline metallic materials. This law attributes the hindering effect of the grain boundaries to the movement of dislocations during plastic deformation [53]. The existence of phases and IMCs in the interior of the grain cannot be neglected for their contribution to the resistance to dislocation motion. For this reason, recent works [54–56] have proposed Hall–Petch type correlations relating the tensile properties to the length scale of other characteristic microstructural features, such as interphase and dendritic arm spacings.

Overall, the σ_y and σ_u values of the investigated alloy ingot are higher than those reported for pure Bi, that is, 7 and 13 MPa, respectively [19]. In the range associated with both a coarser microstructure as well as morphological wavy instabilities for the eutectic Bi–Ni alloy, σ_u and σ_y increased 32% and 6%, respectively, as compared to the corresponding values of pure Bi. On the other hand, for $47.6\,\mu m$ ($0.145\,\mu m^{-1/2}$) $< \lambda <$ $135.2\,\mu m$ ($0.086\,\mu m^{-1/2}$), more significant increase in both σ_u and σ_y can be noted, reaching up to 79% and 149%, respectively, compared to pure Bi. This can be attributed to the effect of the Bi_3Ni IMCs located between the Bi plates acting as a reinforcing phase. In particular, the lower the λ values, the more homogeneously distributed would be the Bi_3Ni particles with a consequential more efficient role in the blocking of dislocations slip. Recently, Peng and Deng [57,58], investigated the mechanical behavior of a Sn–Bi/graphene nanocomposite using finite element method, microhardness and shear stress tests, with a view to analyzing it's application as a thermal interface material. The authors observed that the graphene reinforcement plays an important role in blocking the motion of dislocations, which is in agreement with the classical concept of one of the strengthening mechanisms based on impeding further dislocation propagation with second phases acting as pinning points [59]. This behavior may also be attributed to the Bi_3Ni IMCs located between the Bi plates acting as a reinforcing phase.

4. Conclusions

The following conclusions can be drawn from the present experimental investigation:

- Although the typical microstructure that prevailed along the entire length of the eutectic Bi–Ni alloy ingot was shown

to be characterized by a plate-like structure, morphological wavy instabilities in the Bi plates were shown to occur for $\dot{T} \leq 0.13\,^{\circ}C/s$.

- The X-ray diffraction (XRD) results, as well as the observations made between Bi plates, clearly revealed the presence of the Bi_3Ni IMC, which appears to play a key role in the improvement of both σ_u and σ_y values of the investigated alloy as compared to those reported for pure Bi (increase of up to 79% and 149%, respectively).
- While σ_u and σ_y values remain practically constants in the region of morphological wavy instabilities ($\lambda \geq 142\,\mu m$), Hall–Petch-type correlations are proposed relating the yield and ultimate tensile strengths to λ in a range of microstructural spacings from 47.6 to 135.2 μm.

Conflicts of interest

The authors declare no conflicts of interest.

Acknowledgments

The authors acknowledge CNPq – National Council for Scientific and Technological Development, CAPES – Coordenação de Aperfeiçoamento de Pessoal de Nível Superior – Brasil and FAPESP – São Paulo Research Foundation (grant: 2017/15158-0) for the financial support, as well as the Brazilian Nanotechnology National Laboratory – LNNano for the use of X-ray diffractometer and scanning electron microscope.

REFERENCES

[1] Oguntala G, Abd-Alhameed R, Ngala M. Transient thermal analysis and optimization of convective-radiative porous fin under the influence of magnetic field for efficient microprocessor cooling. Int J Therm Sci 2019;145:1–11, http://dx.doi.org/10.1016/j.ijthermalsci.2019.106019.

[2] Lv L, Dai W, Li A, Lin C-T. Graphene-based thermal interface materials: an application-oriented perspective on architecture design. Polymers (Basel) 2018;10:1–10, http://dx.doi.org/10.3390/polym10111201.

[3] Hansson J, Nilsson TMJ, Ye L, Liu J. Novel nanostructured thermal interface materials: a review. Int Mater Rev 2018;63:22–45, http://dx.doi.org/10.1080/09506608.2017.1301014.

[4] Razeeb KM, Dalton E, Cross GLW, Robinson AJ. Present and future thermal interface materials for electronic devices. Int Mater Rev 2017;63:1–21, http://dx.doi.org/10.1080/09506608.2017.1296605.

[5] Tong XC. Advanced materials for thermal management of electronic packaging. 1st ed. New York: Springer; 2011, http://dx.doi.org/10.1007/978-1-4419-7759-5.

[6] Roy CK, Bhavnani S, Hamilton MC, Johnson RW, Nguyen JL, Knight RW, et al. Investigation into the application of low melting temperature alloys as wet thermal interface materials. Int J Heat Mass Transfer 2015;85:996–1002, http://dx.doi.org/10.1016/j.ijheatmasstransfer.2015.02.029.

[7] Gao Y, Liu J. Gallium-based thermal interface material with high compliance and wettability. Appl Phys A Mater Sci Process 2012;107:701–8, http://dx.doi.org/10.1007/s00339-012-6887-5.

[8] Swamy MCK, Satyanarayan A. Review of the performance and characterization of conventional and promising thermal interface materials for electronic package applications. J Electron Mater 2019;48:7623–34, http://dx.doi.org/10.1007/s11664-019-07623-7.

[9] Yang E, Guo H, Guo J, Shang J, Wang M. Thermal performance of low-melting-temperature alloy thermal interface materials. Acta Metall Sin (English Lett 2014;27:290–4, http://dx.doi.org/10.1007/s40195-014-0042-6.

[10] Hamdan A, McLanahan A, Richards R, Richards C. Characterization of a liquid–metal microdroplet thermal interface material. Exp Therm Fluid Sci 2011;35:1250–4, http://dx.doi.org/10.1016/j.expthermflusci.2011.04.012.

[11] RoHS. Directive 2002/95/EC of the European Parliament and of the council of 27 January 2003 on the restriction of the use of certain hazardous substances in electrical and electronic equipment. Off J Eur Union 2003;46:19–23. https://eur-lex.europa.eu/legal-content/EN/TXT/?uri=CELEX%3A32002L0095 [accessed 12 November 2019].

[12] Poudel B, Hao Q, Ma Y, Lan Y, Minnich A, Yu B, et al. High-thermoelectric performance of nanostructured bismuth antimony telluride bulk alloys. Science (80-) 2008;320:634–8, http://dx.doi.org/10.1126/science.1156446.

[13] Nayek P, Li G. Superior electro-optic response in multiferroic bismuth ferrite nanoparticle doped nematic liquid crystal device. Sci Rep 2015;5:1–9, http://dx.doi.org/10.1038/srep10845.

[14] Ďuran I, Entler S, Kočan M, Kohout M, Viererbl L, Mušálek R, et al. Development of Bismuth Hall sensors for ITER steady state magnetic diagnostics. Fusion Eng Des 2017;123:690–4, http://dx.doi.org/10.1016/j.fusengdes.2017.05.142.

[15] Yu T, Lu S, Xu W, He G. Fabrication of bismuth superhydrophobic surface on zinc substrate. J Solid State Chem 2018;262:26–37, http://dx.doi.org/10.1016/j.jssc.2018.02.019.

[16] Freitas ES, Silva AP, Spinelli JE, Casteletti LC, Garcia A. Inter-relation of microstructural features and dry sliding wear behavior of monotectic Al–Bi and Al–Pb alloys. Tribol Lett 2014;55:111–20, http://dx.doi.org/10.1007/s11249-014-0338-8.

[17] Septimio RS, Arenas MA, Conde A, Garcia A, Cheung N, Damborenea J. Correlation between microstructure and corrosion behaviour of Bi–Zn solder alloys. Corros Eng Sci Technol 2019;54:362–8, http://dx.doi.org/10.1080/1478422X.2019.1600836.

[18] Spinelli JE, Silva BL, Garcia A. Microstructure, phases morphologies and hardness of a Bi–Ag eutectic alloy for high temperature soldering applications. Mater Des 2014;58:482–90, http://dx.doi.org/10.1016/j.matdes.2014.02.026.

[19] Song J-M, Chuang H-Y, Wen T-X. Thermal and tensile properties of Bi–Ag alloys. Metall Mater Trans A Phys Metall Mater Sci 2007;38A:1371–5, http://dx.doi.org/10.1007/s11661-007-9138-1.

[20] Septimio RS, Costa TA, Vida TA, Garcia A, Cheung N. Interrelationship of thermal parameters, microstructure and microhardness of directionally solidified Bi–Zn solder alloys. Microelectron Reliab 2017;78:100–10, http://dx.doi.org/10.1016/j.microrel.2017.08.007.

[21] Demidchik AV, Shepelevich VG. Thermal stability of Bi–Sb (8–12 at% Sb) foils prepared by rapid solidification. Inorg Mater 2004;40:391–4, http://dx.doi.org/10.1023/B:INMA.0000023962.72563.15.

[22] Witusiewicz VT, Hecht U, Rex S, Apel M. In situ observation of microstructure evolution in low-melting Bi–In–Sn alloys by light microscopy. Acta Mater 2005;53:3663–9, http://dx.doi.org/10.1016/j.actamat.2005.04.015.

[23] Song J-M, Chuang H-Y, Wu Z-M. Interfacial reactions between Bi–Ag high-temperature solders and metallic substrates. J Electron Mater 2006;35:1041–9, http://dx.doi.org/10.1007/BF02692565.

[24] Liu Y, Liu S, Zhang C, Lu X, Chen C, Du Y, et al. Thermodynamic assessment of the Bi–Ni and Bi–Ni–X (X = Ag, Cu) systems. J Electron Mater 2016;45:1041–56, http://dx.doi.org/10.1007/s11664-015-4272-9.
[25] Sheikhi R, Cho J. Growth kinetics of bismuth nickel intermetallics. J Mater Sci Mater Electron 2018;29:19034–42, http://dx.doi.org/10.1007/s10854-018-0029-6.
[26] Dybkov VI, Duchenko OV. Growth kinetics of compound layers at the nickel–bismuth interface. J Alloys Compd 1996;234:295–300, http://dx.doi.org/10.1016/0925-8388(95)02096-9.
[27] Lee MS, Chen C, Kao CR. Formation and absence of intermetallic compounds during solid-state reactions in the Ni–Bi system. Chem Mater 1999;11:292–7, http://dx.doi.org/10.1021/CM980521+.
[28] Kumar J, Kumar A, Vajpayee A, Gahtori B, Sharma D, Ahluwalia PK, et al. Physical property and electronic structure characterization of bulk superconducting Bi3Ni. Supercond Sci Technol 2011;24:1–7, http://dx.doi.org/10.1088/0953-2048/24/8/085002.
[29] Piñeiro ELM, Herrera BLR, Escudero R, Bucio L. Possible coexistence of superconductivity and magnetism in intermetallic NiBi3. Solid State Commun 2011;151:425–9, http://dx.doi.org/10.1016/j.ssc.2011.01.005.
[30] Kumar P, Dutta I, Raj R, Renavikar M, Wakharkar V. Novel liquid phase sintered solders with indium as minority phase for next generation thermal interface material applications. In: II Int Conf Therm Issues Emerg Technol. Cairo: IEEE; 2008. p. 325–32, http://dx.doi.org/10.1109/THETA.2008.5167182.
[31] Santos WLR, Cruz CB, Spinelli JE, Cheung N, Garcia A. Tailoring microstructure, tensile properties and fracture process via transient directional solidification of Zn–Sn alloys. Mater Sci Eng A 2018;712:127–32, http://dx.doi.org/10.1016/j.msea.2017.11.039.
[32] Spinelli JE, Cheung N, Goulart PR, Quaresma JMV, Garcia A. Design of mechanical properties of Al-alloys chill castings based on the metal/mold interfacial heat transfer coefficient. Int J Therm Sci 2012;51:145–54, http://dx.doi.org/10.1016/j.ijthermalsci.2011.08.014.
[33] Xavier MGC, Cruz CB, Kakitani R, Silva BL, Garcia A, Cheung N, et al. Directional solidification of a Sn–0.2Ni solder alloy in water-cooled copper and steel molds: Related effects on the matrix micromorphology, nature of intermetallics and tensile properties. J Alloys Compd 2017;723:1039–52, http://dx.doi.org/10.1016/j.jallcom.2017.06.329.
[34] Kakitani R, Reyes RV, Garcia A, Spinelli JE, Cheung N. Relationship between spacing of eutectic colonies and tensile properties of transient directionally solidified Al–Ni eutectic alloy. J Alloys Compd 2018;733:59–68, http://dx.doi.org/10.1016/j.jallcom.2017.10.288.
[35] Costa TA, Dias M, Silva C, Freitas E, Silva AP, Cheung N, et al. Measurement and interrelation of length scale of dendritic microstructures, tensile properties, and machinability of Al–9 wt% Si–(1 wt% Bi) alloys. Int J Adv Manuf Technol 2019:105, http://dx.doi.org/10.1007/s00170-019-04211-1.
[36] Bertelli F, Brito C, Ferreira IL, Reinhart G, Nguyen-Thi H, Mangelinck-Noël N, et al. Cooling thermal parameters, microstructure, segregation and hardness in directionally solidified Al–Sn–(Si;Cu) alloys. Mater Des 2015;72:31–42, http://dx.doi.org/10.1016/j.matdes.2015.02.006.
[37] Gündüz M, Çadirli E. Directional solidification of aluminium–copper alloys. Mater Sci Eng A 2002;327:167–85, http://dx.doi.org/10.1016/S0921-5093(01)01649-5.
[38] Çadırlı E, Büyük U, Engin S, Kaya H. Effect of silicon content on microstructure, mechanical and electrical properties of the directionally solidified Al-based quaternary alloys. J Alloys Compd 2017;694:471–9, http://dx.doi.org/10.1016/j.jallcom.2016.10.010.
[39] Okamoto T, Kishitake K. Dendritic structure in unidirectionally solidified aluminum, tin, and zinc base binary alloys. J Cryst Growth 1975;29:137–46, http://dx.doi.org/10.1016/0022-0248(75)90217-1.
[40] Ma D, Li Y, Ng SC, Jones H. Unidirectional solidification of Zn-rich Zn–Cu peritectic alloys – I. Microstructure selection. Acta Mater 2000;48:419–31, http://dx.doi.org/10.1016/S1359-6454(99)00365-1.
[41] Ma D, Li Y, Ng SC, Jones H. Unidirectional solidification of a Zn-rich Zn–2.17 wt%Cu hypo-peritectic alloy. Sci Technol Adv Mater 2001;2:127–30, http://dx.doi.org/10.1016/S1468-6996(01)00038-9.
[42] Xu W, Feng YP, Li Y, Zhang GD, Li ZY. Rapid solidification behavior of Zn-rich Zn–Ag peritectic alloys. Acta Mater 2002;50:183–93, http://dx.doi.org/10.1016/S1359-6454(01)00321-4.
[43] Xu W, Feng YP, Li Y, Li ZY. Cellular growth of Zn-rich Zn–Ag alloys processed by rapid solidification. Mater Sci Eng A 2004;373:139–45, http://dx.doi.org/10.1016/j.msea.2004.01.022.
[44] Santos WLR, Brito C, Bertelli F, Spinelli JE, Garcia A. Microstructural development of hypoeutectic Zn–(10–40)wt%Sn solder alloys and impacts of interphase spacing and macrosegregation pattern on hardness. J Alloys Compd 2015;647:989–96, http://dx.doi.org/10.1016/j.jallcom.2015.05.195.
[45] Brito C, Siqueira CA, Spinelli JE, Garcia A. Effects of cell morphology and macrosegregation of directionally solidified Zn-rich Zn–Cu alloys on the resulting microhardness. Mater Lett 2012;80:106–9, http://dx.doi.org/10.1016/j.matlet.2012.04.095.
[46] Vida TA, Freitas ES, Brito C, Cheung N, Arenas MA, Conde A, et al. Thermal parameters and microstructural development in directionally solidified Zn-rich Zn–Mg alloys. Metall Mater Trans A Phys Metall Mater Sci 2016;47A:3052–64, http://dx.doi.org/10.1007/s11661-016-3494-7.
[47] Chen Z, Wang E, Hao X. Microstructure and orientation evolution in unidirectional solidified Al–Zn alloys. Mater Sci Eng A 2016;667:1–8, http://dx.doi.org/10.1016/j.msea.2016.04.085.
[48] Clarke AJ, Tourret D, Song Y, Imhoff SD, Gibbs PJ, Gibbs JW, et al. Microstructure selection in thin-sample directional solidification of an Al–Cu alloy: in situ X-ray imaging and phase-field simulations. Acta Mater 2017;129:203–16, http://dx.doi.org/10.1016/j.actamat.2017.02.047.
[49] Oliveira R, Kakitani R, Ramos LR, Gonçalves DL, Garcia A, Cheung N. The roles of Mn and Ni additions to Fe-contaminated Al in neutralizing Fe and stabilizing the cellular α-Al microstructure. J Sustain Metall 2019:1–20, http://dx.doi.org/10.1007/s40831-019-00248-4.
[50] Lima TS, Gouveia GL, Septimio RS, Cruz CB, Silva BL, Brito C, et al. Sn-0.5Cu(-x)Al solder alloys: microstructure-related aspects and tensile properties responses. Metals (Basel) 2019;9:241, http://dx.doi.org/10.3390/met9020241.
[51] Cruz CB, Kakitani R, Xavier MGC, Silva BL, Garcia A, Cheung N, et al. Transient unidirectional solidification, microstructure and intermetallics in Sn–Ni alloys. Mater Res 2018;21:1–11, http://dx.doi.org/10.1590/1980-5373-MR-2017-1099.
[52] Dias M, Brito C, Bertelli F, Garcia A. Cellular growth of single-phase Zn–Ag alloys unidirectionally solidified. Mater Chem Phys 2014;143:895–9, http://dx.doi.org/10.1016/j.matchemphys.2013.11.030.
[53] Hall EO. The deformation and ageing of mild steel. III. Discussion of results. P Phys Soc 1951;64:747–53, http://dx.doi.org/10.1088/0370-1301/64/9/303.
[54] Gouveia GL, Kakitani R, Gomes LF, Afonso CRM, Cheung N, Spinelli JE. Slow and rapid cooling of Al–Cu–Si ultrafine

eutectic composites: interplay of cooling rate and microstructure in mechanical properties. J Mater Res 2019;34:1381–94, http://dx.doi.org/10.1557/jmr.2018.495.
[55] Kakitani R, Reyes RV, Garcia A, Cheung N, Spinelli JE. Effects of melt superheating on the microstructure and tensile properties of a ternary Al–15 wt pct Si–1.5 wt pct Mg alloy. Metall Mater Trans A 2019;50:1308–22, http://dx.doi.org/10.1007/s11661-018-5058-5.
[56] Vida TA, Brito C, Lima TS, Spinelli JE, Cheung N, Garcia A. Near-eutectic Zn–Mg alloys: interrelations of solidification thermal parameters, microstructure length scale and tensile/corrosion properties. Curr Appl Phys 2019;19:582–98, http://dx.doi.org/10.1016/j.cap.2019.02.013.
[57] Peng Y, Deng K. Study on the mechanical properties of the novel Sn–Bi/graphene nanocomposite by finite element simulation. J Alloys Compd 2015;625:44–51, http://dx.doi.org/10.1016/j.jallcom.2014.11.110.
[58] Peng Y, Deng K. Fabrication of reduced graphene oxide nanosheets reinforced Sn–Bi nanocomposites by electro-chemical deposition. Compos Part A Appl S 2015;73:55–62, http://dx.doi.org/10.1016/j.compositesa.2015.03.006.
[59] Callister WD. Materials science and engineering: an introduction. 7th ed. New York: John Wiley & Sons; 2007.